LAWRENCE
LIVERMORE
NATIONAL
LABORATORY

LLNL-PROC-735701

Freezing hydrogen in nanoconfinement

S. O. Kucheyev

July 26, 2017

Target Fabrication Meeting
Las Vegas, NV, United States
March 14, 2017 through March 14, 2017

Disclaimer

Freezing hydrogen in nanoconfinement

S. O. Kucheyev* and J. M. Lenhardt
Lawrence Livermore National Laboratory, Livermore, California 94550, USA
(Dated: July 20, 2017)

Liquid hydrogen confined in pores of nanofoams crystallizes at lower temperatures than in the unconfined, bulk state. Here, we summarize results of our systematic relaxation calorimetry studies of the liquid–solid phase transition of hydrogen and deuterium in various materials with open-cell pores. These include spinodal-decomposition-derived silica glasses and "nanoporous gold," conventional silica aerogels, and carbon foams with ligaments made from nanotubes and graphene sheets. We also present new hydrogen thermoporometry data for dicyclopentadiene (DCPD) aerogels. Results show that hydrogen freezing temperatures inside all the porous materials studied are depressed. The average depression of the freezing point scales linearly with the ratio of the internal surface area to the pore volume. The average freezing point depression is limited to ~ 1.6 K for foams with monolith densities $\lesssim 50$ mg cm^{-3}. Details of the freezing behavior, however, depend non-trivially on the choice of the porous material and on the hydrogen filling fraction, reflecting phenomena that are beyond the Gibbs-Thomson formalism and pointing to the complexity of pore architectures in the low-density materials of interest to thermonuclear fusion energy applications.

I. INTRODUCTION

Hydrogen is the fuel of choice in both inertial confinement fusion (ICF) and magnetic confinement fusion approaches to controlled thermonuclear fusion applications.[1,2] The fuel is typically an equimolar mix of deuterium and tritium, providing the highest fusion reaction cross-section. In most ICF schemes,[2] the fuel is contained inside a spherical ablator capsule as a conformal layer on the inner wall of the capsule. Some ICF target designs call for hydrogen confined inside low-density porous scaffolds. We we will refer to such scaffolds as foams, independent of whether these porous materials are made by foaming or by some other methods. Foams in ICF capsules can be used (i) to define the geometry of the fuel layer; (ii) to control hydrogen crystallization and, hence, the fuel layer roughness; (iii) to introduce dopants inside the fuel layer (for example, for neutron capture diagnostics); (iv) to control capsule fuel filling by condensation inside pores; and (v) to increase or decrease the hydrogen vapor pressure inside the capsule central cavity when the fuel is at temperatures above or below the freezing point, respectively.[2]

The confinement of hydrogen in foams influences both its thermodynamic properties and crystallization kinetics. Here, we summarize results of our recent relaxation calorimetry studies of the liquid-solid phase transition of H_2 and D_2 confined in various foams, ranging from spinoidal-decomposition-derived nanoporous glasses to graphene foams.[3–7] We illustrate the relaxation calorimetry method by presenting new data for the crystallization of H_2 confined in polymeric dicyclopentadiene (DCPD) foams, which are candidate materials for some target designs.[8,9]

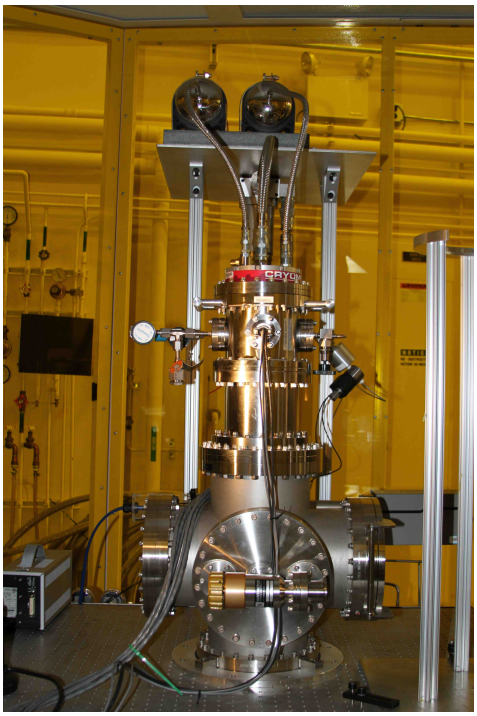

FIG. 1. Photograph of the cryostat assembly.

II. EXPERIMENT

The synthesis and some basic properties of the DCPD foams investigated here were described in detail by Lenhardt et al.[9] We studied the so called NB_2NB system of DCPD.[9] An average monolith density of 20 mg cm^{-3} was determined by measuring the dimensions and mass of the monolith. A specimen with a total mass of 9 mg was used for thermoporometry measurements reported here. The liquid–solid phase transition was monitored by relaxation calorimetry with condensed H_2 filling the pores as opposed to conventional thermoporometry based

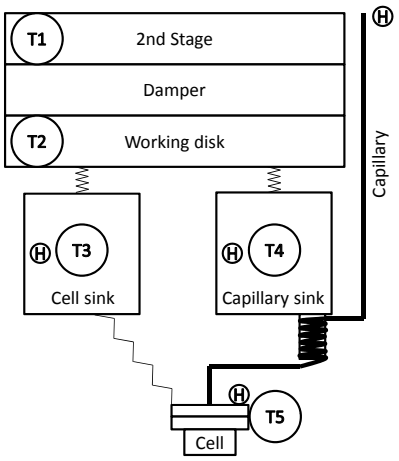

FIG. 2. Schematic of the relaxation calorimeter for studies of freezing and melting of hydrogens confined in porous materials. Heaters and thermometers are labeled as "H" and "T", respectively. Zigzag lines show controlled thermal links.

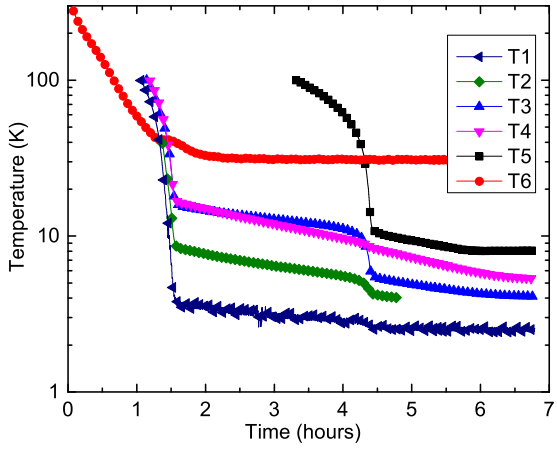

FIG. 3. Temporal evolution of thermometer readings during a typical cool down of the cryostat. The labels in the legend correspond to the thermometers labeled in Fig. 2, while "T6" refers to a thermometer mounted on the 1st stage of the cryostat.

on differential scanning calorimetry or nuclear magnetic resonance and water as the pore filling liquid.[10,11] Figure 1 shows a photograph of the cryostat assembly, which includes a vertically positioned pulse tube refrigerator hosted in a 6-way cross chamber. The refrigerator with a feedthrough collar are connected to the chamber via an 8-inch conflat flange and are disconnected and removed from the chamber during each sample exchange. To minimize vibrations, the 6-way cross chamber is bolted to an optical table, and the pulse tube motor is mounted on a separate support. The H_2 gas used was obtained from Matheson Tri-Gas with a purity of $\gtrsim 99.999\%$ and natural isotopic content. Additional details of this custom built calorimeter can be found in Ref. 3.

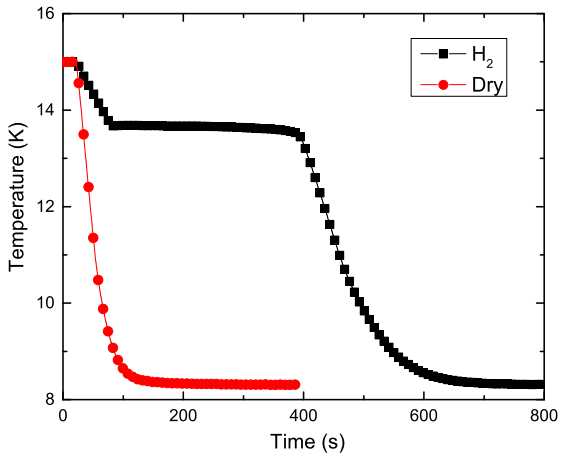

FIG. 4. Temporal evolution of temperature of the calorimeter cell with a DCPD aerogel on cooling when the cell heater is turned off (at 20 s). Shown are curves for both a "dry" cell (i.e., the cell with a DCPD specimen without H_2) and the cell with the DCPD aerogel filled with H_2. For clarity, only every 10th experimental point is displayed.

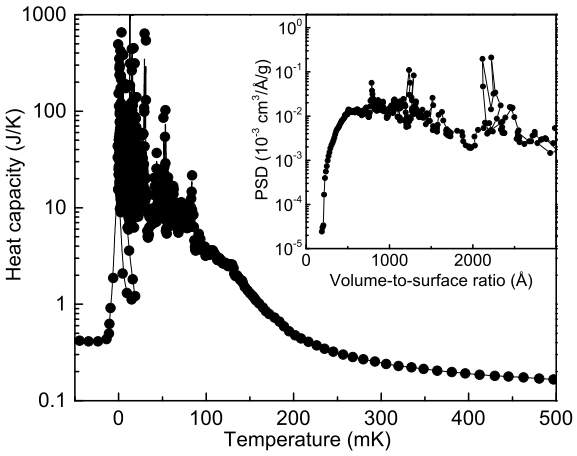

FIG. 5. (Color online) Temperature dependence of the effective heat capacity of H_2 inside a DCPD aerogel measured on cooling. The temperature is referenced to the freezing point of bulk (unconfined) H_2. The inset shows the pore size distribution (PSD) derived from the temperature dependence of the heat capacity as described in the text.

Figure 2 shows a schematic of the key calorimeter components thermally anchored to the 2nd stage of the cryostat. Figure 3 illustrates typical calorimeter cool down curves, showing readings of the thermometers labeled in Fig. 2 and an additional thermometer mounted on the 1st stage of the cryostat. It is seen from Fig. 3 that, although the 1st and 2nd stages of the cryostat approach their base temperatures of ~ 30 and ~ 3 K, respectively, within $\sim$ 1.5 hours, the cool down of the calorimeter cell itself takes much longer due to a weak thermal link between the cell and its sink (which is essential for relaxation calorimetry measurements). As a result, the

cryostat cool down takes $\sim$ 5 hours before H_2 can be admitted and relaxation calorimetry measurements performed. Figure 3 also illustrates that the noisy signal of the 2nd stage (the T1 trace) is smoothed out by the stainless steel damper disk (see Fig. 2) so that the the working disk, both heat sinks, and the cell have a temperature stability of $\sim$ 1 mK.

III. RESULTS AND DISCUSSION

The relaxation calorimetry on cooling (i.e., freezing) is based on accurate measurements of the temporal evolution of calorimeter cell temperature after the cell heater is turned off when heat flows from the cell via a weak thermal link to the cell sink, which is kept at a constant temperature (labeled "T3" in Fig. 2). In our experiments, the capillary sink temperature (labeled "T4" in Fig. 2) was also kept the same as T3 although the thermal design ensured that the heat flow along the stainless steel capillary from the cell to the capillary sink was negligible.

Figure 4 shows an example of the temporal evolution of cell temperature (T5 in Fig. 2) with a DCPD aerogel for a "dry" cell (i.e., without H_2) and for a cell with a DCPD aerogel filled with H_2. This DCPD specimen was overfilled with H_2 prior to cooling in order to allow the crystallization front to invade the aerogel pores from outside the monolith, minimizing undercooling events. It is seen from Fig. 4 that a relaxation time constant of a dry cell is $\sim$ 1 minute. This time constant can be readily controlled by selecting a different size of the thermal link between the cell and the cell sink or by changing the temperature of the cell sink (T3). Figure 4 also shows that, when the foam is filled H_2, the cooling proceeds much slower due to an additional heat capacity of H_2 and the latent heat of the liquid–solid phase transition. A plateau of the $T(t)$ scan at 13.7 K in Fig. 4 reflects the freezing of liquid H_2 outside the aerogel monolith. The freezing of H_2 confined inside the pores of the DCPD aerogel occurs at lower temperatures, which is evidenced as a change in the first derivative of $T(t)$ curves.

The temperature dependence of the effective heat capacity of H_2, $C(T)$, can be calculated from $T(t)$ scans such as shown in Fig. 4 according to a procedure described in detail in Ref. 7. This analysis is based on the fact that C is inversely proportional to $\frac{dT}{dt}$. Hence, a change in the slope of $T(t)$ scans reflects the latent-heat-related contribution to the otherwise smoothly varying $C(T)$ dependence of H_2. Figure 5 shows the $C(\Delta T)$ dependence derived from the $T(t)$ scan of Fig. 4. We plot C as a function of relative temperature, $\Delta T = T^m_{bulk} - T$, since the freezing temperature of H_2 depends on its ortho-para composition.[1,2] Here, T^m_{bulk} is the equilibrium liquid–solid phase transition temperature of the unconfined material. In our previous studies,[3,4] we have not found any evidence of effects of orthohydrogen content on the shape of the $C(T)$ dependence. Hence, we reference the temperature scale to T^m_{bulk} and refer to it as relative temperature.

In Fig. 5, the freezing of H_2 confined in nanopores is revealed by latent-heat-related peaks positioned over a smoothly varying background caused by the strong $C(T)$ dependence of H_2. It is seen that nanoconfined H_2 freezes at lower temperatures than bulk H_2, with the tail of the $C(\Delta T)$ curve extending to $\sim$ 300 mK below the bulk freezing point. Such a depression of the freezing temperature of a nanoconfined liquid is a thermodynamic rather than kinetic effect. It is caused by an additional energy of the interface between a frozen solid inside the pores and a premolten layer on pore walls.[3–7,10,11] The freezing point depression is related to the pore size via a Gibbs-Thomson equation:[7]

$$\Delta T_{freeze} = \frac{T^m_{bulk}\sigma_{sl}}{\rho_l \Delta H}\frac{S}{V} = \frac{\gamma}{D}, \qquad (1)$$

where ρ_l is the density of the liquid, σ_{sl} is the solid–liquid surface energy, ΔH is the latent heat of crystallization, γ is a constant combining all of the parameters related to the liquid confined, and D is an effective pore size defined as $D = \frac{V}{S}$, where V is the pore volume and S is the surface area of pores.

In addition, $C(T)$ dependencies can be used to calculate pore size distributions (PSDs), $\frac{dV}{dD}(D)$, as follows:[6]

$$\frac{dV}{dD} = \frac{C_{latent}\Delta T^2}{\Delta H \gamma \rho_l m}, \qquad (2)$$

where m is the mass of the nanoporous specimen and C_{latent} is the contribution of the latent heat of crystallization to the total effective heat capacity measured, which we calculate by subtracting a smoothly varying background from $C(T)$ curves. In Eqs. 1 and 2, constant values of $\gamma = 66$ Å K, $\Delta H = 117$ J mol^{-1}, and $\rho_l = 3.83 \times 10^4$ mol m^{-3} were used (with γ taken from Ref. 7 and ΔH and ρ_l from Refs. 12 and 13, respectively). The inset in Fig. 5 shows a PSD obtained by such an analysis. It reveals a broad curve straddling from $D \approx 200$ Å (corresponding to $\Delta T \approx 300$ mK, according to Eq. 1) to $D \gtrsim 2000$ Å. The region of larger Ds is obscured by the presence of undercooling events evidenced as large spikes in the $C(T)$ and PSD dependencies. Such undercooling events occurring inside pores have been discussed in detail previously.[5,6] Results of Fig. 5 are consistent with expectations[6,7] that the the average pore size for these DCPD foams is $D = \frac{V}{S} \approx 1400$ Å, where $S = 350$ m^2 g^{-1} (Ref. 9) and $V = \frac{1}{\rho} - \frac{1}{\rho_{lig}} = 49$ cm^3 g^{-1}, with $\rho = 20$ mg cm^{-3} and $\rho_{lig} = 0.98$ g cm^{-3} being densities of the DCPD monolith and the material of ligaments in the foam, respectively.

The above results and those from Refs. 3–7 allow us to make predictions of the average freezing depression temperature (ΔT_{freeze}) of hydrogens. Based on a previous comparative study of the freezing of H_2 and D_2 is silica aerogels and extrapolation to tritium containing hydrogens with the quantum law of corresponding

states,[5] ΔT_{freeze} is expected to be the same for D_2 and DT. This allows us to make estimates of ΔT_{freeze} for DT based on much less technically demanding experiments with nanoconfined D_2. For both D_2 and DT confined in a low-density nanoporous matrix with given ρ and S (that could be readily measured by conventional methods such as weighing specimens of with known volumes and by gas sorption, respectively), the average freezing temperature depression is

$$\Delta T_{freeze} = 5.3 \times 10^{-6} \times S\rho, \quad (3)$$

where S and ρ are in commonly used units of m^2 g^{-1} and mg cm^{-3}, respectively.[6] Therefore, for low-density foams of interest as ICF fuel scaffolds with $\rho < 50$ mg cm^{-3}, the average ΔT_{freeze} is limited to ~ 1.6 K even for foams with theoretically maximum surface areas of ~ 6000 m^2 g^{-1}.[6] These are, however, estimates for *average* ΔT_{freeze}. Broad PSDs reflecting local density fluctuations in the foam could lead to cases when the fuel in parts of the foam pore volume remains liquid at much lower temperatures. In addition, not all surface area of pores measured by, for example, gas sorption[14] contributes to the freezing point depression given by Eq. 1. Indeed, as discussed in detail elsewhere,[6] small pores with $D \lesssim 20$ Å do not contribute to ΔT_{freeze} estimates. Thus, the average ΔT_{freeze} could actually be smaller than that predicted by Eq. 3 for materials with a large fraction of micropores.[6] Additional complexity (and additional flexibility in the ICF target design) arises for aerogel scaffolds with incompletely filled pores, which exhibit lower ΔT_{freeze} than those estimated by Eq. 1.[5] These effects deserve further systematic studies.

IV. SUMMARY

In summary, we have used high-resolution relaxation calorimetry to study the freezing behavior of H_2 confined in a DCPD aerogel with a monolith density of 20 mg cm^3. The depression of the freezing temperature of H_2 in this aerogel occurs over a range of temperatures down to ~ 300 mK below the bulk freezing point. This aerogel is characterized by a broad pore size distribution with pore sizes larger than ~ 2000 Å. Based on these and previous results,[3–7] the depression of the average freezing point of DT in a low density nanoporous scaffold can be estimated with Eq. 3.

V. ACKNOWLEDGMENTS

This work was performed under the auspices of the U.S. DOE by LLNL under Contract DE-AC52-07NA27344.

* kucheyev@llnl.gov

[1] P. C. Souers, *Hydrogen Properties for Fusion Energy* (University of California Press, Berkeley, 1986).
[2] S. O. Kucheyev and A. V. Hamza, J. Appl. Phys. **108**, 091101 (2010).
[3] E. Van Cleve, M. A. Worsley, and S. O. Kucheyev, Rev. Sci. Instrum. **84**, 053901 (2013).
[4] S. O. Kucheyev, E. Van Cleve, and M. A. Worsley, J. Phys.: Condens. Matter **26**, 225004 (2014).
[5] E. Van Cleve, M. A. Worsley, and S. O. Kucheyev, J. Appl. Phys. **116**, 163517 (2014).
[6] S. O. Kucheyev, E. Van Cleve, L. T. Johnston, S. A. Gammon, and M. A. Worsley, Langmuir **31**, 3854 (2015).
[7] L. T. Johnston, M. M. Biener, J. C. Ye, T. F. Baumann, and S. O. Kucheyev, J. Appl. Phys. **118**, 025303 (2015).
[8] S. H. Kim, M. A. Worsley, C. A. Valdez, S. J. Shin, C. Dawedeit, T. Braun, T. F. Baumann, S. A. Letts, S. O. Kucheyev, K. J. J. Wu, J. Biener, J. H. Satcher, Jr., and A. V. Hamza, RSC Advances **2**, 8672 (2012).
[9] J. M. Lenhardt, S. H. Kim, M. A. Worsley, R. N. Leif, P. G. Campbell, T. F. Baumann, and J. H. Satcher, Jr., J. Non-Cryst. Solids **408**, 98 (2015).
[10] H. K. Christenson, J. Phys.: Condensed Matter **13**, R95 (2001).
[11] O. V. Petrov and I. Furo, Prog. Nucl. Mag. Res. Spec. **54**, 97 (2009).
[12] R. F. Dwyer, G. A. Cook, B. M. Shields, and D. H. Stellrecht, J. Chem. Phys. **42**, 3809 (1965).
[13] R. D. Goodwin, D. E. Diller, H. M. Roder, and L. A. Weber, Cryogenics **2**, 81 (1961).
[14] S. Brunauer, P. H. Emmett, and E. Teller, J. Am. Chem. Soc. **60**, 309 (1938).